ORBITAL SOLUTIONS OF BINARY WHITE DWARF MERGER SYSTEMS

by

S. Roffe

Bachelor of Science, University of Pittsburgh, 2017

Submitted to the Graduate Faculty of

the Department of Physics and Astronomy in partial fulfillment

of the requirements for the degree of

Bachelor of Philosophy

University of Pittsburgh

2017

UNIVERSITY OF PITTSBURGH

UNIVERSITY OF PITTSBURGH, DEPARTMENT OF PHYSICS AND ASTRONOMY

This dissertation was presented

by

S. Roffe

It was defended on

March 31st 2017

and approved by

Dr. Carles Badenes, University of Pittsburgh Department of Physics and Astronomy

Dr. Tom Matheson, National Optical Astronomy Observatory

Dr. Michael Wood-Vasey, University of Pittsburgh Department of Physics and Astronomy

Dr. Andrew Zentner, University of Pittsburgh Department of Physics and Astronomy

Dissertation Director: Dr. Carles Badenes, University of Pittsburgh Department of Physics and Astronomy

ORBITAL SOLUTIONS OF BINARY WHITE DWARF MERGER SYSTEMS

S. Roffe, Bphil

University of Pittsburgh, 2017

We present follow-up observations to white dwarf binary candidates that were identified by spectral variability in SDSS by Badenes Maoz (2012). We obtained multiple spectra of 24 systems at the Mayall 4m telescope at Kitt Peak, which we analyzed using a Markov Chain Monte Carlo method to measure radial velocities with realistic error bars. Among these systems 6 present strong evidence for binarity, and for these 6 systems we derive orbital solutions.

TABLE OF CONTENTS

LIST OF FIGURES

LIST OF TABLES

1.0 INTRODUCTION

1.1 WHITE DWARF SYSTEMS

A vast majority of stars with masses below 8 $M_\odot$ end their lives as degenerate white dwarfs (WDs). Some WDs are in close binary systems where they interact with their companions, leading to a plethora of astrophysical phenomena, from cataclysmic variables and nova explosions to Type Ia Supernovae. A particularly interesting aspect of these binary systems is the outcome of the merging process at the end of their binary evolution. When two CO WDs merge, a thermonuclear runaway may be triggered and eventually lead to a Type Ia supernova (SNe Ia) explosion (Iben Tutukov 1984, Webbink 1984). SNe Ia play an important role in modern astronomy. Their light curves have a correlation between luminosity and brightness, which makes them useful as a "standard candle" to track distances in the expanding universe. This scenario, known as a double degenerate WD SNe Ia progenitor scenario, has been the incentive to search for such merger system candidates (Badenes et al. 2009).

1.2 MERGER TIME

Despite the fact that WD binaries are abundant (Nelemans et al. 2005, Napiwotzki et al. 2007, Holberg et al. 2016), only a small fraction of them are considered potential SN Ia progenitors. Only the systems with merger time less than a Hubble time are assumed to be SN Ia progenitors. The currently measured merger rate in the Milky Way is $(7 \pm 2) \times 10^{-13} \mathrm{yr}^{-1} \mathrm{M}_\odot^{-1}$

(Badenes and Maoz 2012, Maoz Hallakoun 2017). Pre-merging systems must have an orbital period of less than ∼12 hours. This limits the number of progenitors greatly, so it is important to identify and characterize all systems that fit this criterion.

1.3 SPECTRA CONSIDERED

The spectra of double degenerate systems generally resemble those of single WDs because the light from one of the stars usually dominates the flux at optical wavelengths. In these cases, the presence of a companion white dwarf is inferred from radial velocity (RV) measurements of the photometric primary, which involve quantifying the Doppler shift around the Balmer lines in the optical spectrum. The target is identified as a binary through statistical model selection comparisons.

In this paper, we present follow-up observations to white dwarf binary candidates identified by spectral variability in the Sloan Digital Sky Survey (SDSS) by Badenes Maoz (2012). We obtained multiple spectra of 24 systems at the Mayall 4m telescope at Kitt Peak, which we analyzed using a Markov Chain Monte Carlo method to measure radial velocities with realistic error bars. Among these systems 6 present strong evidence for binarity, and for these 6 systems we derive orbital solutions.

2.0 OBSERVATIONS AND TARGET SELECTION

The targets were selected by cross-correlating the sub-exposures of all the spectra classified as WDs by the SDSS pipeline (up to DR7) to identify objects with RV shifts. Objects classified as WDs with M dwarf companions in the catalogs of Eisenstein et al. (2006) and Rebassa-Mansergas et al. (2010) were culled out of the target list.

Interesting double degenerate systems are expected to have orbital periods between 1 hour and 1 day. Each object was observed continuously for 1-2 hours with individual exposures between 10 and 20 minutes, and then the observing time was alternated between the objects for the remainder of the run. In this way, the observations are sensitive to both long and short orbital periods. Observations were spread over the course of 4 days in order to account for any possible weather interference.

3.0 METHODS

The data was collected at the 4m Mayall telescope at Kitt Peak National Observatory 4m by Carles Badenes and Tom Matheson. Spectra were taken in 10 to 20 minute exposures of 24 star systems, between 14 and 30 exposures for each system. The spectra were reduced by Tom Matheson. The reduced spectra were normalized by masking out the broad Balmer absorption lines and interpolating. Because the spectra span between 3800 and 5220 Angstroms, we used the normalized H beta, H gamma, and H delta lines in each spectrum. We measure radial velocities by fitting them with a simplified Voigt profile, a Lorentzian with a Gaussian core, using the Markov chain Monte Carlo (MCMC) solver `emcee` (Foreman-Mackey et al. 2013). The Voigt profile uses five free parameters: Gaussian width and depth, Lorentzian width and depth, and the radial velocity shift. The Gaussian and Lorentzian depths and widths were determined by first fitting a stationary atmosphere model to a stationary Voigt with four free parameters (Koester 2010). Then, with the widths and depths, the radial velocity fitting was determined by one free parameter, namely the radial velocity. All three hydrogen lines were fit jointly by locking the radial velocity shift between them. The median of the MCMC posterior in velocity space then becomes the measured RV, with the range containing 68.3% of the posterior area being the 1σ confidence interval. Typical error found for cleaner spectra was ~90-110 km s^{-1}, demonstrated in Figures 4 and 5. Error for noisier spectra typically fell into the region of ~150-200 km s^{-1}, as shown in Figures 6 and 9.

Radial velocity measurements from spectra with a signal to noise ratio below 3.0 were ignored to avoid outliers. The remaining RVs were then fitted with a sine curve using the same Markov chain Monte Carlo methodology to determine an orbital solution for each system. To determine if the system is truly a binary, the Akaike information criterion (AIC) is

calculated for the sine fit and compared to a constant radial velocity model.

The use of MCMC methodology in our RV measurements allows for a realistic estimate of the measurement error, which is commonly underestimated using traditional chi-squared minimization techniques.

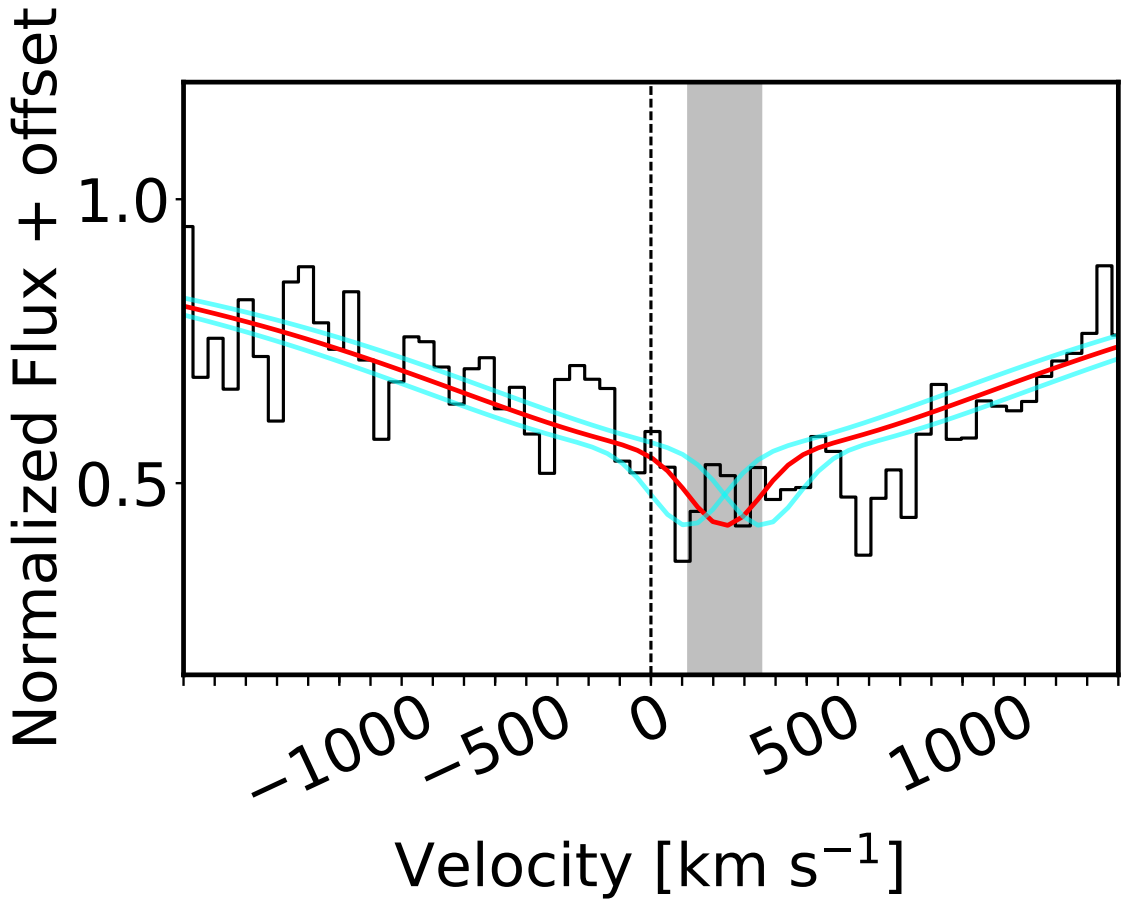

Figure 1: An example of a radial velocity fit for J123549.89+154319.3 using a Voigt profile. One standard deviation around the best fit is highlighted in gray.

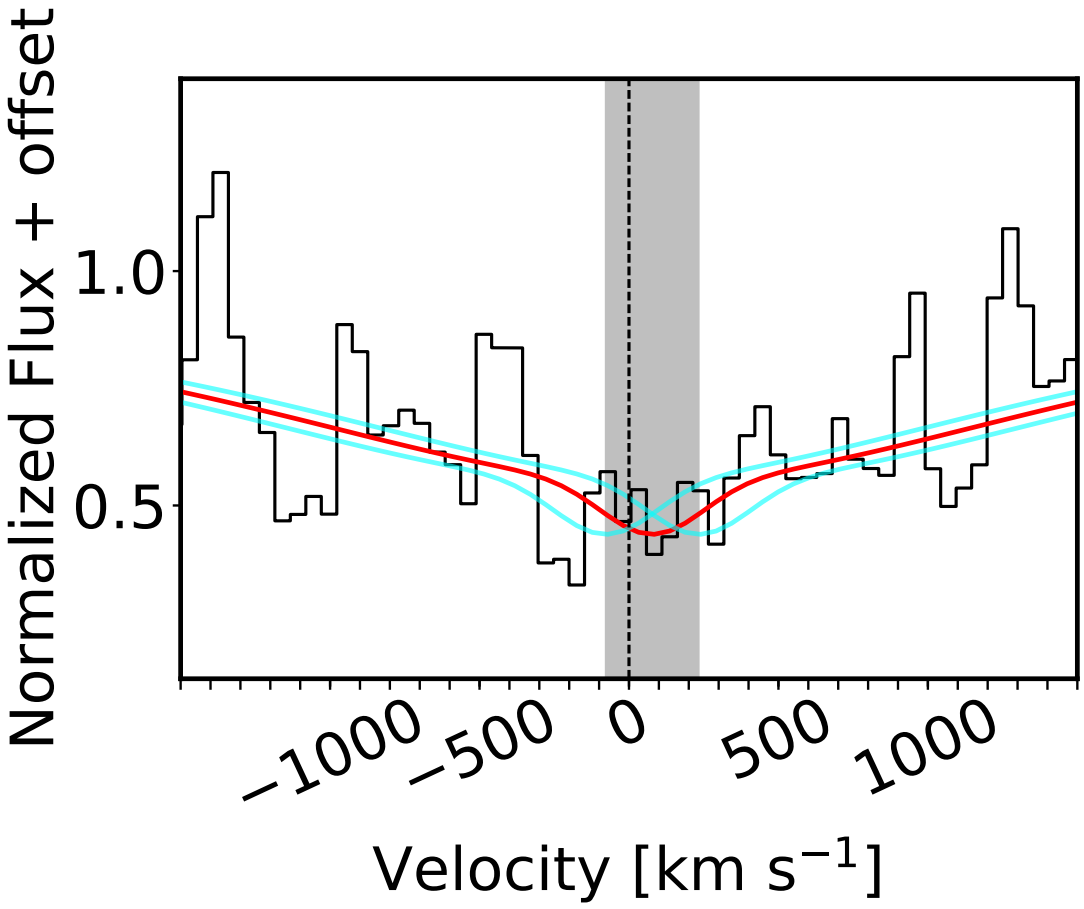

Figure 2: An example of a radial velocity fit for a noisier spectrum for J112105.25+644336.2.

4.0 BINARITY MODEL SELECTION

4.1 MODELS USED

The binarity of the targets were determined using the difference in AIC measured for a binary sinusoidal orbit and a constant radial velocity model. The four parameters for the sinusoidal model, namely period, amplitude, angular offset and vertical offset, were determined by fitting the radial velocity points to a sine model using MCMC. The measured radial velocities are shown in Table 4, including the MJD of the midpoint of the observation. For 7 of these binaries, we obtained enough data to measure the orbital periods fairly accurately displayed in figures 4 through 9. For these fits, we assume that the orbits are circular with the model,

$$v(t) = Ksin(2\pi(t - P) + \phi) + \gamma$$

with P being the measured orbital period, K being the amplitude of the radial velocity, and ϕ and γ being some angular and vertical offset, respectively. To see if the radial velocities measured were due to noise, the constant radial velocity was determined by taking a weighted average of the radial velocity measurements, $\sum_i \frac{v_i \sigma_i^{-2}}{\sigma_i^{-2}}$ where σ_i is the error on the radial velocity measurement v_i with variance $\frac{1}{\sum_i \sigma_i}$.

4.2 AIC

The AIC was used to test how well both models fit with the data whilst considering the complexity of the model in the number of parameters. The AIC calculation was defined to be

$$AIC = -2ln(L^0(M)) + 2k + \frac{2k(k+1)}{N-k-1}$$

where L^0 is the maximized likelihood function of the model M, k is the number of parameters, and N is the total number of data points. The value ΔAIC was defined to be $AIC_{const} - AIC_{sine}$ where AIC_{const} was the AIC calculated for the constant radial velocity model, and AIC_{sine} was the AIC calculated for the binary sinusoidal model, so that the larger ΔAIC is, the more confident we are that the system is a binary. A fiducial value for a confident detection of binarity was chosen to be $\Delta AIC >= 300$ corresponding to a confidence of $\geq 95\%$.

The full list of observed targets and their prospective AIC measurements are listed in Table 1.

Table 1: AIC Calculations for all observed targets sorted from largest to smallest ΔAIC

Object	Num of Observations	ΔAIC
J123549.89+154319.3	23	2888.93
J234902.80+355301.0	22	2153.02
J114024.02+661842.2	18	679.58
J034319.09+101238.0	25	659.01
J120315.22+650524.4	14	536.09
J112105.23+644336.4	14	394.37
J130646.51+152224.9	19	282.24
J111501.16-124217.9	16	260.04
J090751.78+071844.6	21	259.15
J152125.02+391536.5	18	236.72
J222903.69+122928.6	22	203.00
J165923.87+643809.3	26	174.83
J085921.90+043812.3	18	170.40
J011721.34+311650.9	23	168.02
J020439.19+220724.7	29	167.05
J074904.33+422420.0	21	163.13
J140327.76+002119.5	20	160.38
J205118.90+031209.4	23	121.61
J113709.84+003542.9	15	77.35
J151132.20+451732.6	7	71.92
J154126.42+371647.6	3	43.81
J091215.43+011958.8	8	35.84
J133137.06+010632.3	6	-0.22
J030941.46+005259.4	6	-0.99

5.0 RESULTS: BINARITY AND ORBITAL FITS

We observed a total of 24 systems, which had between 6 and 29 spectra of sufficient quality to measure RVS. The AIC criterion singled out 6 of these systems as binaries, and for these we display the best fit orbital solutions below in Figures 3-8.

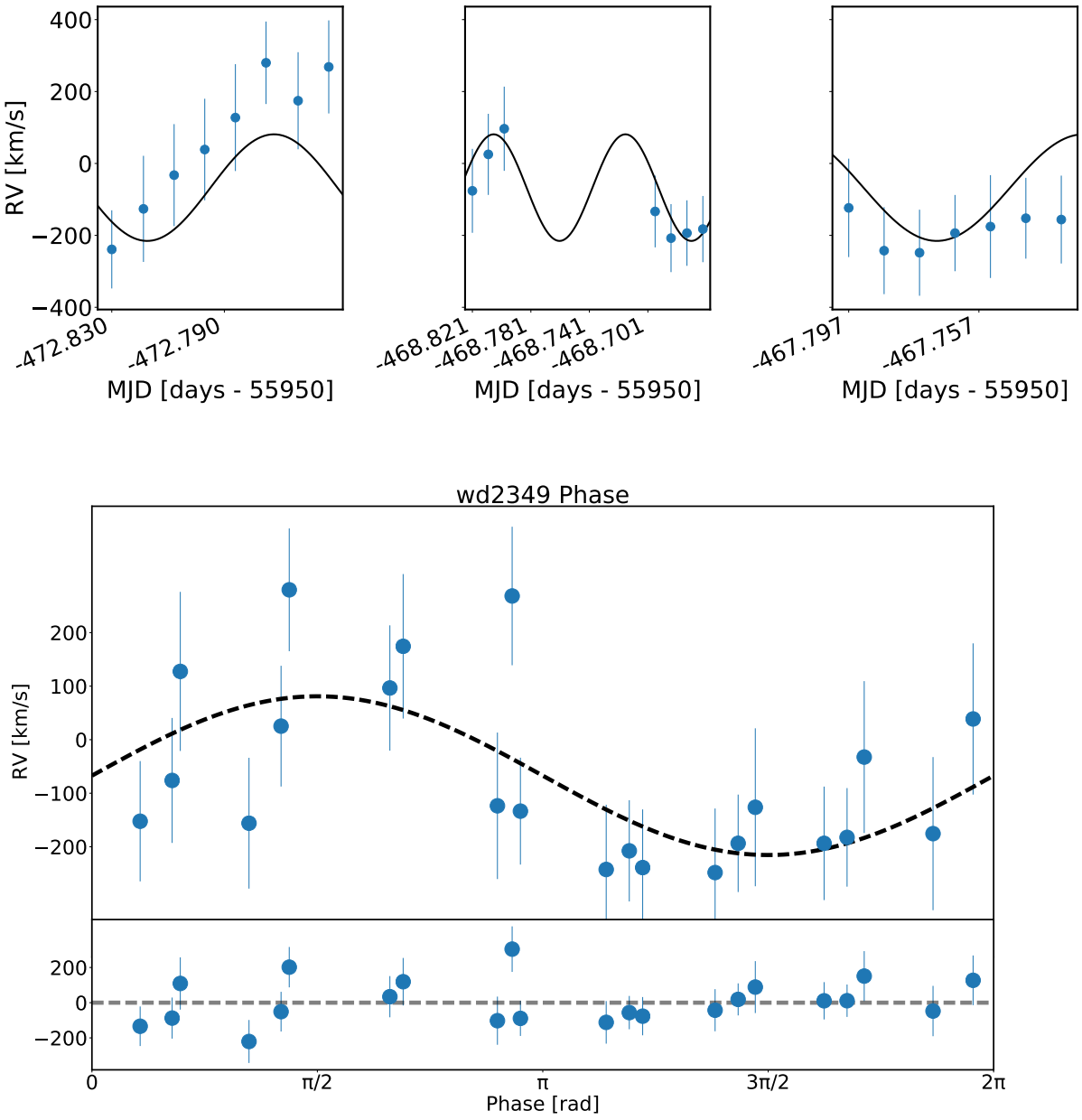

Figure 3: Radial velocities and the best-fit orbit for J234902.80+355301.0. The bottom panel shows all of the data points phased with the best-fit period with residuals.

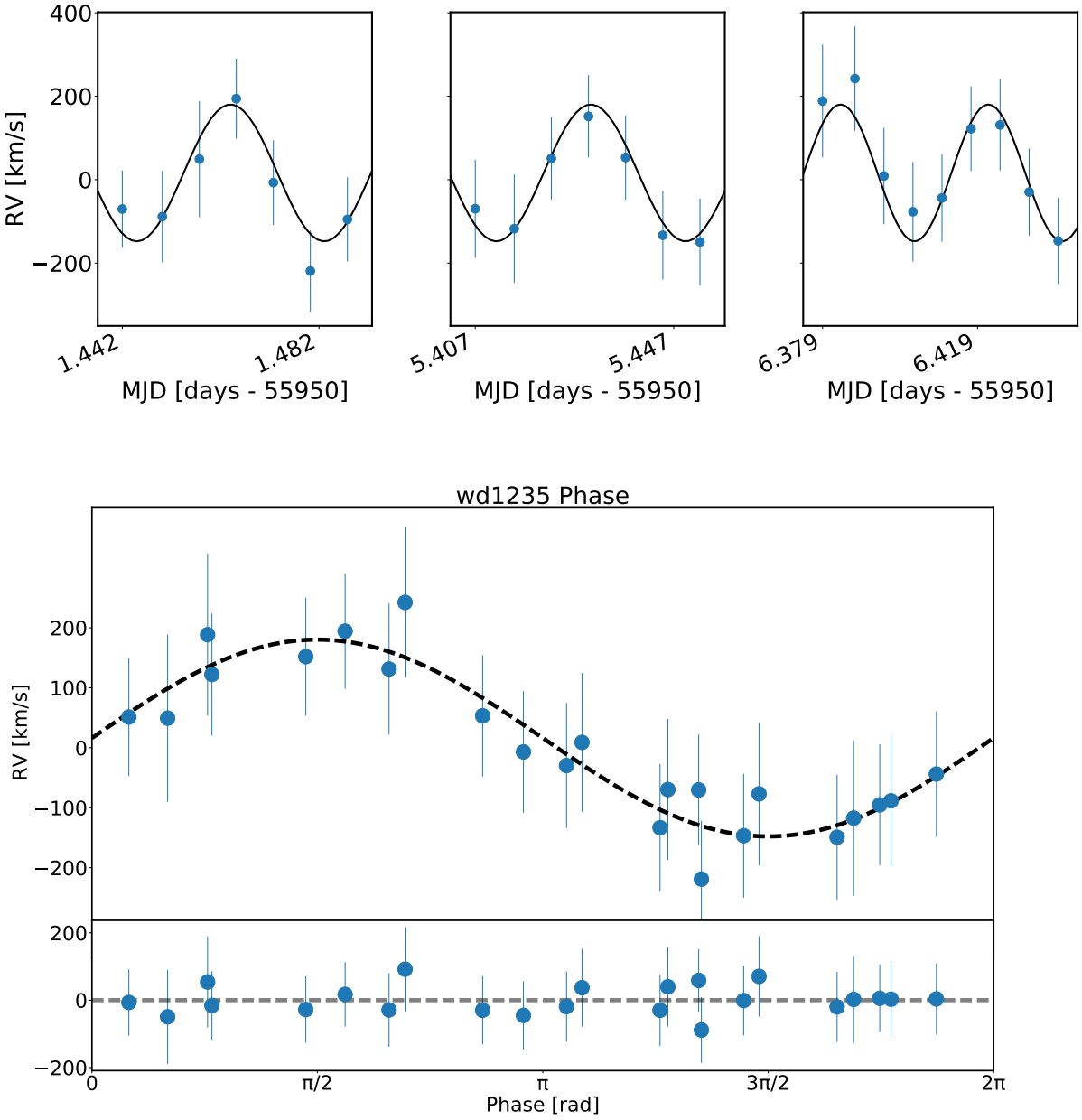

Figure 4: Same as figure 4 but for J123549.89+154319.3.

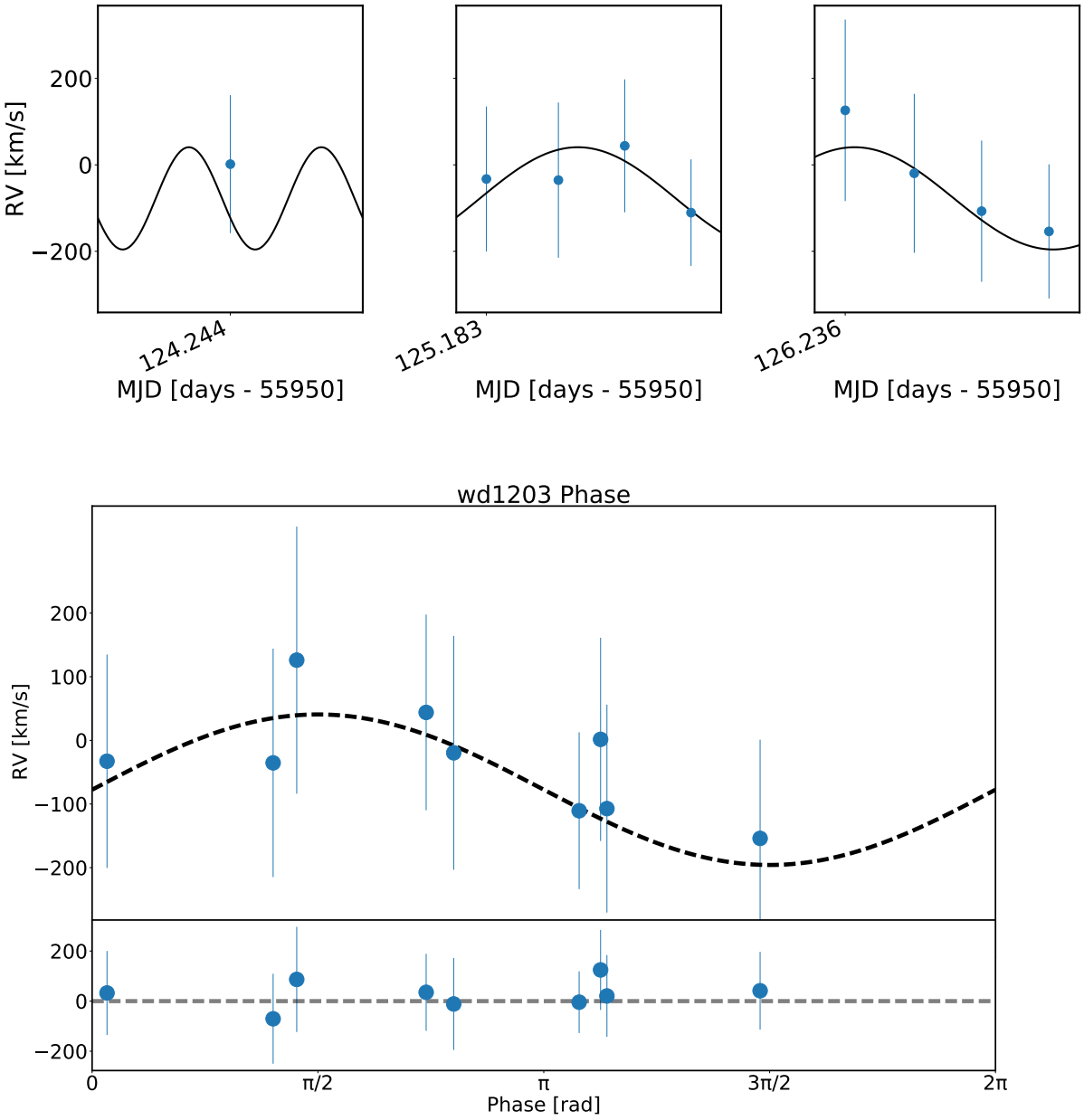

Figure 5: Same as Figure 1, but for J120315.22+650524.4.

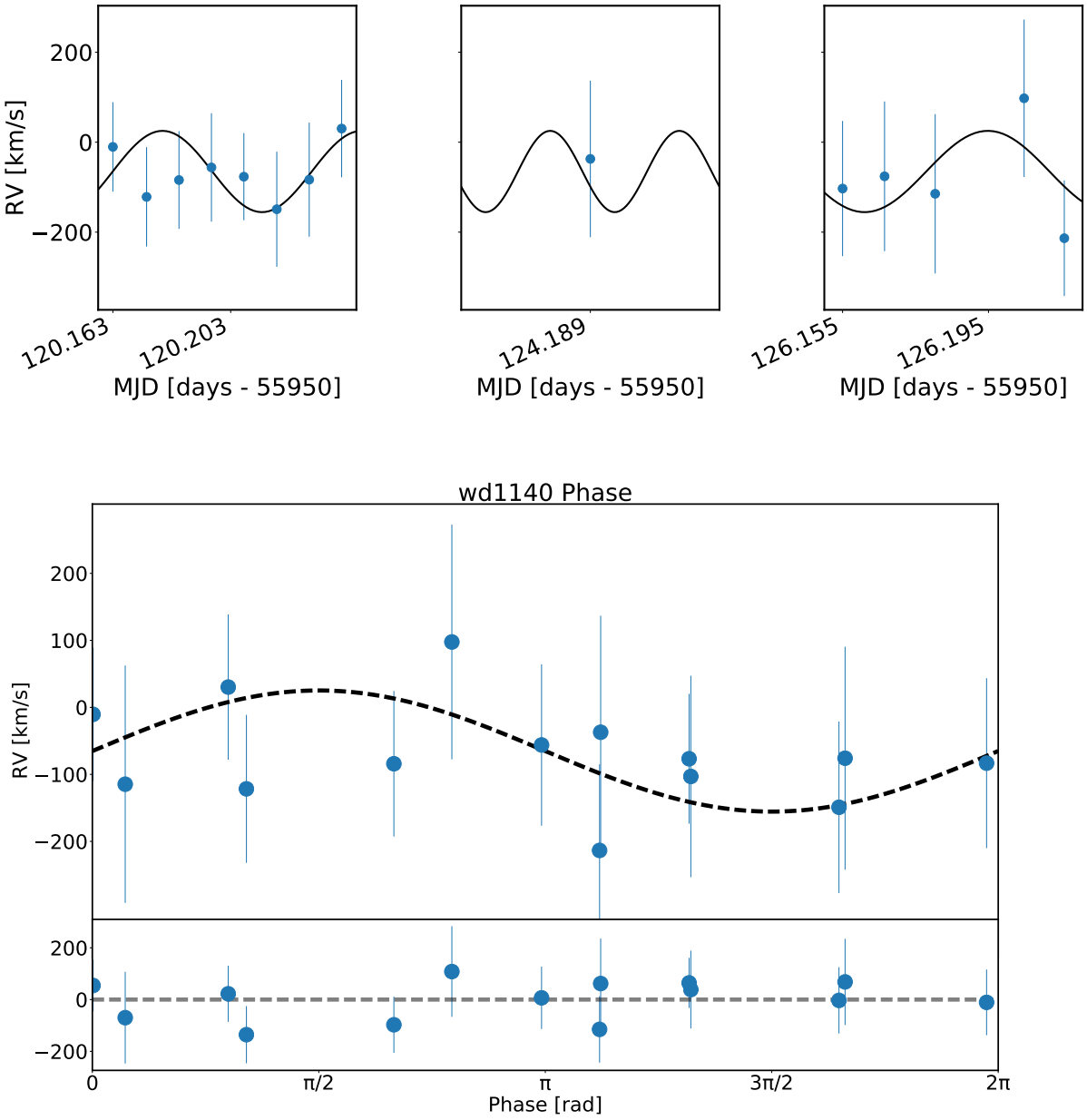

Figure 6: Same as Figure 1, but for J114024.02+661842.2.

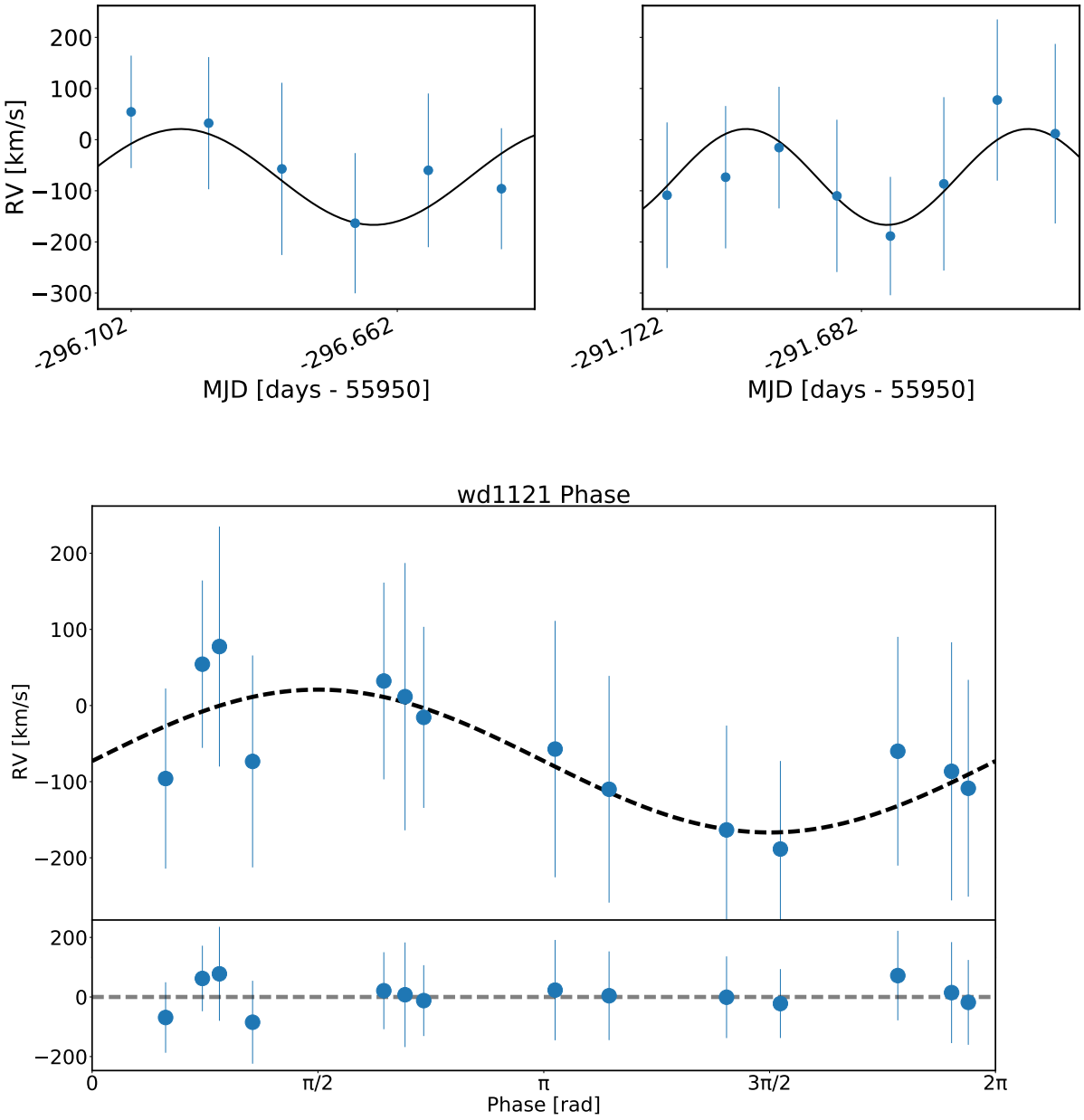

Figure 7: Same as Figure 1, but for J112105.23+644336.4.

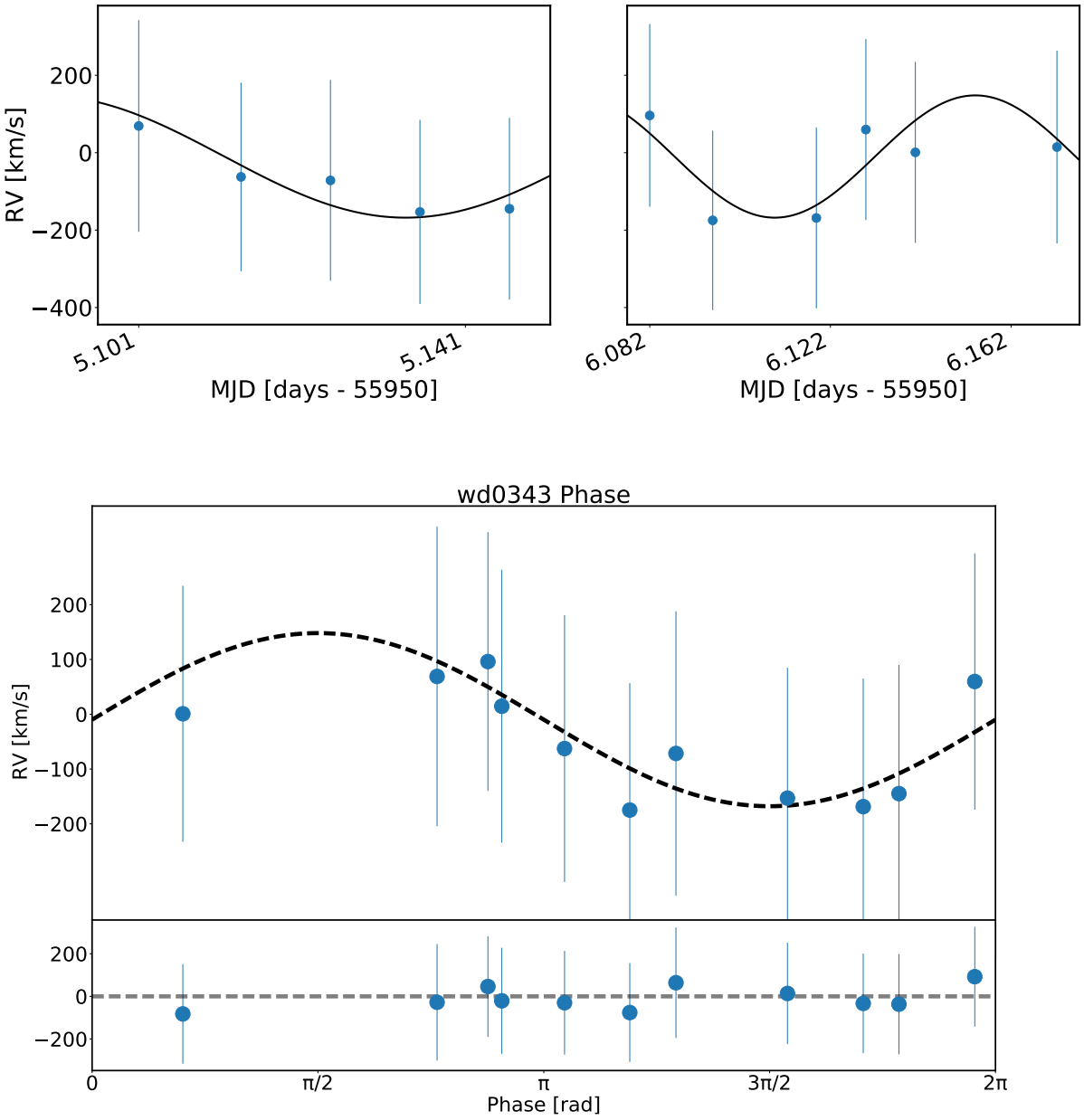

Figure 8: Same as Figure 1, but for J034319.09+101238.0.

Table 2: Orbital Fit Parameters

Object	Amplitude [km s^{-1}]	Period [days]	ϕ [rad]	γ [km s^{-1}]
J034319.09+101238.0	157.94 ± 6.47	$8.88E-02 \pm 2.10E-03$	6.16 ± 1.82	−9.89 ± 4.84
J112105.25+644336.2	93.81 ± 4.48	$5.80E-02 \pm 1.16E-03$	5.79 ± 1.82	−72.93 ± 3.24
J114024.02+661842.3	90.38 ± 3.92	$6.76E-02 \pm 9.22E-03$	3.46 ± 1.84	−65.17 ± 2.86
J120315.22+650524.4	118.28 ± 5.02	$6.50E-02 \pm 1.39E-03$	3.01 ± 1.81	−77.54 ± 4.42
J123549.89+154319.3	164.00 ± 3.49	$3.81E-02 \pm 6.69E-04$	1.02 ± 1.82	16.22 ± 2.66
J234902.80+355301.0	148.24 ± 3.31	$9.01E-02 \pm 3.48E-03$	4.25 ± 1.83	−67.19 ± 3.41

6.0 WHITE DWARF MASSES

For each target, we fit the log g and effective surface temperature, T_{eff} to a grid of atmosphere cooling models where $g = \frac{GM}{R^2}$ is the surface gravity of the white dwarf. The cooling models used for mass measurement are described in detail in Holberg Bergeron 2006, Kowalski Saumon 2006, Tremblay et al. 2011, and Bergeron et al. 2011. Only those describing "thick" H and He shells were used for CO core models due to the abundance of thick H and He shells compared to thin shells. The log g and T_{eff} values were obtained from the Kleinman et al. 2013 catalog. The log g and T_eff were then fit to the cooling models to obtain a mass for the primary white dwarf.

Using this mass of the primary white dwarf, a minimum mass for the companion star, assuming the orbital inclination $i = 90°$ was obtained by using the binary mass function $f \approx \frac{M_2^3 \sin^3(i)}{M_1^2} = \frac{P_{orb}K^3}{2\pi G}$ where P_{orb} is the measured orbital period, K is the amplitude of the radial velocity, G is the gravitational constant, M_2 is the mass of the companion star, M_1 is the mass of the primary star, and i is the angle of inclination of the orbit.

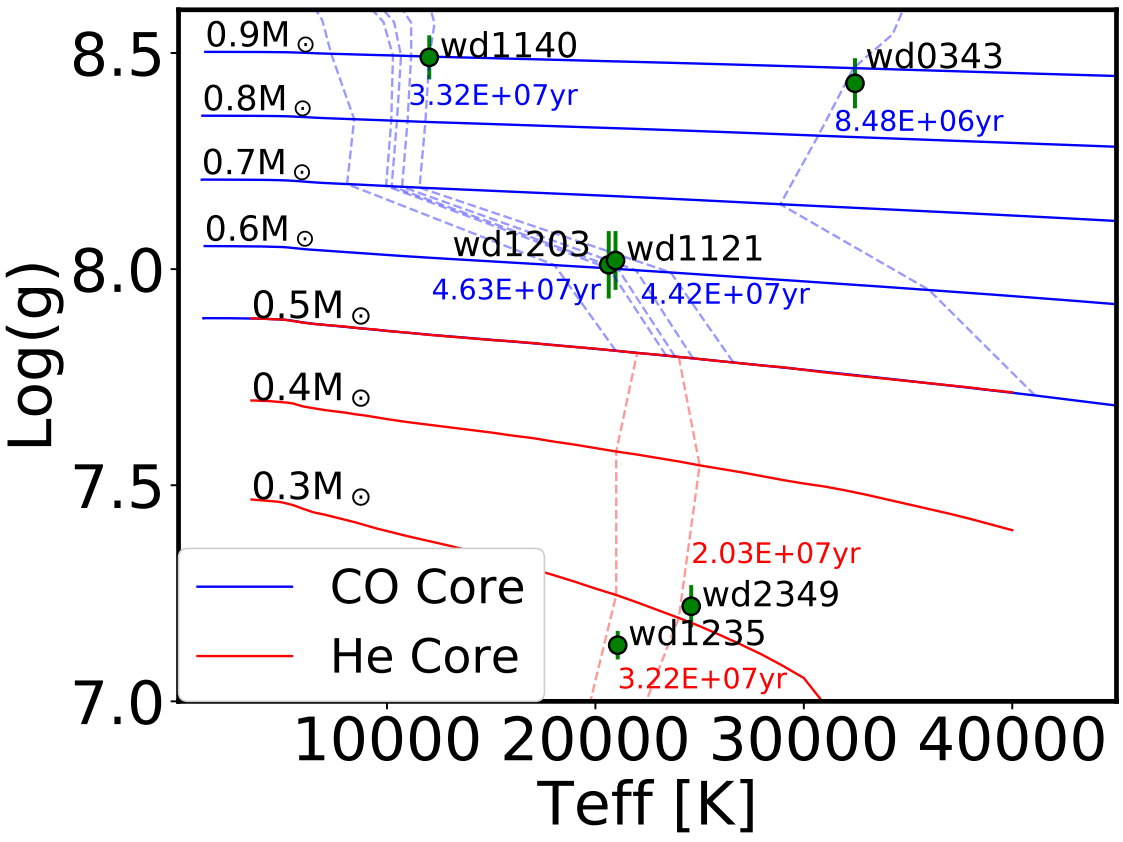

Figure 9: Log of the surface gravity vs. effective surface temperature for each of the targets. The dotted lines depict lines of equal ages. Solid lines represent cooling models. The naming sequence follows "wd" followed by the first four digits of the full target name.

Table 3: Primary and companion white dwarf mass estimates with age estimate.

Object	Primary WD Mass [$M_\odot$]	Minimum Companion Mass [$M_\odot$]	Age [Myr]
J034319.09+101238.0	0.91 ± 0.05	0.31 ± 0.03	8.48 ± 3
J112105.25+644336.2	0.63 ± 0.03	0.13 ± 0.02	44.2 ± 2
J114024.02+661842.3	0.92 ± 0.03	0.16 ± 0.02	33.2 ± 4
J120315.22+650524.4	0.63 ± 0.04	0.16 ± 0.02	46.3 ± 3
J123549.89+154319.3	0.27 ± 0.03	0.11 ± 0.01	32.2 ± 6
J234902.80+355301.0	0.34 ± 0.03	0.15 ± 0.02	20.3 ± 5

7.0 DISCUSSION

Figures 4-9 contain various potential orbital solutions for the targets presented. Because or MCMC measurements yield more realistic RV errors, these orbital solutions appear to be worse than those typically found in the published literature for spectra of similar quality. However, the AIC criteria clearly single out these systems as binaries, and these solutions are the best that can be obtained with the data at hand. The limiting factors here are the telescope aperture and the quantum efficiency of the RC spectrograph that was used to collect the data. This spectrograph has since been refurbished, and an observing campaign similar to ours would likely yield much better results if conducted today.

The six systems presented in this work all have short periods and large amplitudes, and will merge in less than a Hubble time. They join the small but growing sample of known pre-merger WDs, and therefore remain interesting sources to characterize the progenitors of future transients.

Figure 3 contains the surface gravity and effective surface temperature against cooling models. Using the measurements from this figure, and the binary mass function defined above, we can estimate a minimum mass for the companion star by assuming that the angle of inclination, i is 90°. Mass estimations can give us a sense of the mass limits of SNe Ia progenitors. Primary and companion mass measurements can be found in Table 3.

8.0 CONCLUSIONS

In the paper we have presented several targets displaying strong binarity. The use of Marcov chain Monte Carlo statistics led to larger errors than what are typically found. However, this may reflect a more realistic estimation of radial velocity errors. AIC calculation comparisons can allow us to determine with high certainty whether a target is a binary despite larger error values despite larger errors.

Table 4: Radial Velocity Measurements for 234902.80+355301.0

Object	MJD (days)	v_{helio} ($km\ s^{-1}$)
234902.80+355301.0	55477.169833	−238.94 ± 108.67
...	55477.181092	−126.28 ± 147.54
...	55477.191980	−32.45 ± 141.84
...	55477.202865	38.71 ± 141.25
...	55477.213751	127.55 ± 148.59
...	55477.224642	279.97 ± 114.69
...	55477.236030	174.43 ± 134.96
...	55477.246926	268.45 ± 129.38
...	55481.179145	−76.13 ± 116.71
...	55481.190033	25.30 ± 112.79
...	55481.200913	96.57 ± 117.05
...	55481.304103	−133.48 ± 99.82
...	55481.314988	−207.62 ± 94.54
...	55481.325869	−193.58 ± 91.02
...	55481.336758	−182.48 ± 92.06
...	55482.203217	−123.50 ± 136.83
...	55482.214090	−242.47 ± 120.95
...	55482.224977	−248.21 ± 119.66
...	55482.235872	−193.62 ± 106.00
...	55482.246762	−175.51 ± 143.01
...	55482.257640	−152.34 ± 112.35
...	55482.268524	−156.01 ± 122.19

Table 5: RV Measurements for J123549.89+154319.3

Object	MJD (days)	v_{helio} ($km\ s^{-1}$)
J123549.89+154319.3	55951.441858	−58.83 ± 84.09
...	55951.449994	−97.06 ± 96.15
...	55951.457533	26.84 ± 131.44
...	55951.465040	170.80 ± 89.45
...	55951.472581	−0.50 ± 91.33
...	55951.480108	−223.36 ± 92.27
...	55951.487651	−92.50 ± 91.18
...	55955.406668	−59.58 ± 110.88
...	55955.414523	−109.15 ± 119.81
...	55955.422004	28.66 ± 96.75
...	55955.429489	139.99 ± 94.62
...	55955.436968	71.23 ± 94.86
...	55955.444470	−116.05 ± 97.69
...	55955.451958	−136.10 ± 97.90
...	55956.378727	170.36 ± 124.08
...	55956.387080	236.74 ± 118.05
...	55956.394562	18.82 ± 106.89
...	55956.402049	−76.15 ± 111.69
...	55956.409550	−38.06 ± 97.66
...	55956.417045	133.15 ± 97.42
...	55956.424537	138.89 ± 105.34
...	55956.432044	−32.11 ± 98.69
...	55956.439533	−143.93 ± 100.26

Table 6: RV Measurements for J120315.22+650524.4

Object	MJD (days)	v_{helio} ($km\ s^{-1}$)
J120315.22+650524.4	56074.221751	123.53 ± 228.46
...	56074.232754	−161.00 ± 196.56
...	56074.243984	0.85 ± 159.57
...	56074.255000	−276.00 ± 149.68
...	56075.158870	−171.22 ± 198.47
...	56075.170750	112.90 ± 229.87
...	56075.182917	−32.59 ± 167.96
...	56075.194862	−35.36 ± 179.17
...	56075.205867	43.80 ± 153.65
...	56075.216869	−110.38 ± 122.83
...	56076.235947	126.71 ± 209.99
...	56076.247236	−20.79 ± 183.63
...	56076.258254	−109.16 ± 163.12
...	56076.269269	−152.03 ± 154.70

Table 7: RV Measurements for J114024.02+661842.2

Object	MJD (days)	v_{helio} ($km\ s^{-1}$)
J114024.02+661842.2	56070.163368	−11.07 ± 99.43
...	56070.174810	−120.54 ± 110.93
...	56070.185812	−84.14 ± 108.47
...	56070.196829	−56.02 ± 120.21
...	56070.207835	−76.29 ± 96.68
...	56070.219018	−149.64 ± 128.08
...	56070.230031	−83.72 ± 126.72
...	56070.241036	30.28 ± 108.07
...	56074.162953	199.35 ± 156.84
...	56074.176120	66.23 ± 173.73
...	56074.188600	−36.75 ± 173.41
...	56074.199608	−307.91 ± 116.62
...	56076.155216	−103.68 ± 150.45
...	56076.166722	−75.72 ± 165.47
...	56076.180600	−116.15 ± 177.07
...	56076.193487	76.20 ± 155.85
...	56076.204970	97.99 ± 174.81
...	56076.215989	−213.23 ± 128.67

Table 8: RV Measurements for J112105.23+644336.4

Object	MJD (days)	v_{helio} ($km\ s^{-1}$)
J112105.23+644336.4	55653.297648	52.84 ± 109.97
...	55653.309302	32.60 ± 128.73
...	55653.320302	−55.83 ± 168.88
...	55653.331312	−163.12 ± 136.64
...	55653.342311	−60.75 ± 149.96
...	55653.353304	−95.02 ± 117.20
...	55658.278263	−108.76 ± 142.00
...	55658.290316	−74.13 ± 138.97
...	55658.301306	−16.34 ± 118.41
...	55658.313210	−110.48 ± 148.65
...	55658.324211	−188.39 ± 115.12
...	55658.335207	−87.76 ± 169.20
...	55658.346201	77.72 ± 155.91
...	55658.358123	13.41 ± 175.64

Table 9: RV Measurements for J034319.09+101238.0

Object	MJD (days)	v_{helio} ($km\ s^{-1}$)
J034319.09+101238.0	55951.223520	−201.33 ± 199.37
...	55951.235249	−232.59 ± 230.17
...	55951.246269	−112.18 ± 211.02
...	55951.257459	183.33 ± 200.10
...	55955.100523	74.85 ± 271.95
...	55955.113051	−65.15 ± 242.64
...	55955.124002	−73.45 ± 258.62
...	55955.134960	−155.71 ± 235.89
...	55955.145919	−147.25 ± 233.44
...	55955.169506	−97.06 ± 276.56
...	55955.181566	−63.19 ± 261.17
...	55955.192526	200.34 ± 252.44
...	55955.203466	28.50 ± 242.29
...	55955.214431	−55.69 ± 282.14
...	55956.082189	95.68 ± 236.12
...	55956.096132	−177.44 ± 230.34
...	55956.108104	−32.38 ± 276.75
...	55956.119077	−169.91 ± 233.97
...	55956.130040	64.49 ± 233.76
...	55956.140992	2.86 ± 232.24
...	55956.159416	51.95 ± 292.92
...	55956.172342	16.63 ± 248.74
...	55956.183297	−58.97 ± 278.78
...	55956.194256	−142.19 ± 232.59
...	55956.205212	−92.64 ± 281.59

BIBLIOGRAPHY

[1] Carles Badenes and Dan Maoz. The merger rate of binary white dwarfs in the galactic disk. *The Astrophysical Journal Letters*, 749(1):L11, 2012.

[2] Carles Badenes, Fergal Mullally, Susan E Thompson, and Robert H Lupton. First results from the swarms survey. sdss 1257+ 5428: a nearby, massive white dwarf binary with a likely neutron star or black hole companion. *The Astrophysical Journal*, 707(2):971, 2009.

[3] Carles Badenes, Marten H van Kerkwijk, Mukremin Kilic, Steven J Bickerton, Tsevi Mazeh, Fergal Mullally, Lev Tal-Or, and Susan E Thompson. Sdss 1355+ 0856: a detached white dwarf+ m star binary in the period gap discovered by the swarms survey. *Monthly Notices of the Royal Astronomical Society*, 429(4):3596–3603, 2013.

[4] P Bergeron, F Wesemael, Pierre Dufour, A Beauchamp, C Hunter, Rex A Saffer, A Gianninas, MT Ruiz, M-M Limoges, Patrick Dufour, et al. A comprehensive spectroscopic analysis of db white dwarfs. *The Astrophysical Journal*, 737(1):28, 2011.

[5] Daniel J Eisenstein, James Liebert, Hugh C Harris, SJ Kleinman, Atsuko Nitta, Nicole Silvestri, Scott A Anderson, JC Barentine, Howard J Brewington, J Brinkmann, et al. A catalog of spectroscopically confirmed white dwarfs from the sloan digital sky survey data release 4. *The Astrophysical Journal Supplement Series*, 167(1):40, 2006.

[6] D. Foreman-Mackey, D. W. Hogg, D. Lang, and J. Goodman. emcee: The MCMC Hammer. , 125:306, March 2013.

[7] JB Holberg and Pierre Bergeron. Calibration of synthetic photometry using da white dwarfs. *The Astronomical Journal*, 132(3):1221, 2006.

[8] JB Holberg, EM Sion, T Oswalt, GP McCook, S Foran, and John P Subasavage. A new look at the local white dwarf population. *The Astronomical Journal*, 135(4):1225, 2008.

[9] Icko Iben Jr and Alexander V Tutukov. Supernovae of type i as end products of the evolution of binaries with components of moderate initial mass (m not greater than about 9 solar masses). *The Astrophysical Journal Supplement Series*, 54:335–372, 1984.

[10] Mukremin Kilic, Warren R Brown, Carlos Allende Prieto, Marcel Andre Agüeros, Craig Heinke, and SJ Kenyon. The elm survey. ii. twelve binary white dwarf merger systems. *The Astrophysical Journal*, 727(1):3, 2010.

[11] D Koester. White dwarf spectra and atmosphere models. *Memorie della Societa Astronomica Italiana*, 81:921–931, 2010.

[12] PM Kowalski and D Saumon. Found: The missing blue opacity in atmosphere models of cool hydrogen white dwarfs. *The Astrophysical Journal Letters*, 651(2):L137, 2006.

[13] R Napiwotzki, CA Karl, Gijs Nelemans, L Yungelson, N Christlieb, H Drechsel, U Heber, D Homeier, D Koester, B Leibundgut, et al. Binary white dwarfs in the supernova ia progenitor survey. In *15th European Workshop on White Dwarfs*, volume 372, page 387, 2007.

[14] Gijs Nelemans and CA Tout. Reconstructing the evolution of white dwarf binaries: further evidence for an alternative algorithm for the outcome of the common-envelope phase in close binaries. *Monthly Notices of the Royal Astronomical Society*, 356(2):753–764, 2005.

[15] A Rebassa-Mansergas, BT Gänsicke, Matthias R Schreiber, Detlev Koester, and P Rodríguez-Gil. Post-common envelope binaries from sdss–vii. a catalogue of white dwarf-main sequence binaries. *Monthly Notices of the Royal Astronomical Society*, 402(1):620–640, 2010.

[16] P-E Tremblay, P Bergeron, and A Gianninas. An improved spectroscopic analysis of da white dwarfs from the sloan digital sky survey data release 4. *The Astrophysical Journal*, 730(2):128, 2011.

[17] RF Webbink. Double white dwarfs as progenitors of r coronae borealis stars and type i supernovae. *The Astrophysical Journal*, 277:355–360, 1984.